



# TiO<sub>2</sub>/in-situ reduced GO/functionalized with an IL-Cr complex as a ternary photocatalyst composite for efficient carbon monoxide deterioration from air

Naemeh Seifvand, Elaheh Kowsari\*

Department of Chemistry, Amirkabir University of Technology, Hafez Avenue, No. 424, Tehran, Iran

## ARTICLE INFO

### Article history:

Received 16 October 2016

Received in revised form

25 December 2016

Accepted 10 January 2017

Available online 13 January 2017

### Keywords:

TiO<sub>2</sub>

Reduced graphene oxide

Photocatalytic activity

IL-Cr complex

CO degradation

## ABSTRACT

Photocatalyst composed with titanium dioxide (TiO<sub>2</sub>) and reduced graphene oxide (RGO) functionalized with ionic liquid (IL) and chromium (Cr) was created. Characterization techniques, confirming the structure of RGO/IL-Cr( $\eta^6$ -C<sub>6</sub>H<sub>5</sub>), were established by X-ray diffraction, TEM, BET, XPS and FT-IR. The complex was covalently attached on the RGO sheets through an imidazolium-based IL linker. The layered structure of RGO, in combination with the active role of the IL in reaction, makes the synthesized catalyst more efficient for the excellent elimination of CO (97%). Interaction between Cr and CO leads to the corresponding Cr(III) tricarbonyl complex, [Cr(CO)<sub>3</sub>( $\eta^6$ -C<sub>6</sub>H<sub>5</sub>)]. This complex could promote the yield of gas degradation by the reaction of [Cr( $\eta^6$ -C<sub>6</sub>H<sub>5</sub>)] with CO, besides the photocatalyst activity of TiO<sub>2</sub>. Compared with TiO<sub>2</sub>, TiO<sub>2</sub>/RGO/IL-Cr composite develops an almost 3-fold enhancement in the photodegradation rate towards CO under UV irradiation. The improved photocatalytic activity of this ternary system benefits from the synergistic effect between RGO and Cr, which is proven by the photocurrent-time experiments; this improvement facilitates the interfacial charge transfer and simultaneously the CO elimination. The results highlighted the importance of harmonization between charge separations, surface area augmentation and coordination reaction process, and this is important to achieve high photocatalytic efficiency.

© 2017 Elsevier B.V. All rights reserved.

## 1. Introduction

Photocatalysts are key intermediates in environmental applications since they undergo reactions in transforming pollutants to harmless products, benefitting from light energy [1]. The photon energy produces free radicals of  $\bullet$ O<sup>−</sup><sub>2ads</sub> or H<sub>2</sub>O<sub>2</sub> from semiconductors and molecular oxygen. These reactions generate other products such as holes which generate in return OH<sup>•</sup>. These reactive species are initiators of photocatalytic reactions [2–6]. For this purpose, a number of photocatalysts have been explored. These phenomena correspond to a wide variety of metal oxides or semiconductors such as TiO<sub>2</sub>, ZnO, WO [7,8]. Recently, TiO<sub>2</sub> has been given considerable attention in the field of photocatalyst, and this is due to its appropriate aspects, for instance its massive abundance in the nature, its resistance against light or chemical solvents [9,10].

However, other undesirable properties, including the wide band gap, UV light excitation demand, intolerant synthesis procedures, rapid deactivation, and tough catalyst replacement; have limited TiO<sub>2</sub> application perspectives [11–13].

Therefore, it can be advanced that using thin layer of TiO<sub>2</sub>, produced by a fine technique of plasma enhanced chemical vapor deposition (PECVD) may clear up the problem [14,15].

Carbon monoxide (CO) threatens human health by reducing oxygen transport to the body. At enough high levels, CO can be fatal [16]. Many approaches have been proposed to reduce the level of CO in the atmosphere. Photocatalytic degradation of CO has turned out to be promising one, from both environmental and economical viewpoints. In other aspects, CO complexes formation is one of the most efficient strategies for its catching and then eliminating, since these complexes are reasonably stable with large K<sub>f</sub> values, available and inexpensive [17].

As it was explained in a last paper, cobalt complexes were prepared by using covalent linkage of imidazole with GO. Due to the inherent photocatalytic activity and complex formation, remarkable enhancement of air purification was observed over

\* Corresponding author.

E-mail addresses: [kowsarie@aut.ac.ir](mailto:kowsarie@aut.ac.ir), [e.kowsari@yahoo.com](mailto:e.kowsari@yahoo.com) (E. Kowsari).

the catalyst, [18]. Indeed, experimental results confirmed high-percentage deterioration of  $\text{NO}_x$  (51%) and CO (46%). However, some problems still remain to be solved in its application, such as low CO elimination or selectivity of CO in a gas mixture. Therefore, improving photocatalytic activity for CO deterioration has become an issue.

Considering octahedral cluster units, CO molecules are ligands and Cr is a central atom, respectively. Thus, we intended to immobilize a coordination complex onto convenient support for adapting it with  $\text{TiO}_2$  photocatalyst. Surprisingly, chromium (Cr) carbonyl complexes have proven to be stable, with the benefit of CO selectivity in mixed gases [19].

The promising initial work was the motivation in employing graphene as an efficient support for Cr complexes. Graphene belongs to the family of carbon materials; it is arranged in a perfect hexagonal lattice. As a matter of fact, graphene Oxide (GO) has attracted tremendous attention, due to its remarkable inherent specific surface area, perfect charge mobility, and mechanical stability [20]. Subsequently, the chemical structure of GO empowers scientists to functionalize the oxygen groups (hydroxyl, carboxyl and epoxy) which thoroughly exist both in basal plane and sheet edges.

A need arose to reduce GO. RGO is achievable via a chemical modification of GO [21]. In-situ reduction of GO means that there is no need to add a reducing agent or an extra chemical reaction.

The composites of graphene and  $\text{TiO}_2$  nanoparticles have been recognized as efficient heterogeneous catalysts for photocatalytic reactions, due to their layered spaces, providing accessible catalytic active sites [22]. Yinjie Cen et al. have reported  $\text{TiO}_2$ –graphene composite, as a high-performance lithium battery [23]. Mn-doped  $\text{TiO}_2$ , supported on reduced-GO, was performed as a visible active photocatalyst [24]. RGO, with its extended C–C network, is able to store electrons after excitation of  $\text{TiO}_2$  by light [25].

Ionic liquids (ILs) are materials, with bulky organic cation and organic or inorganic anion. Besides, ILs have many sustainable properties, including very minor vapor pressure, low melting points, excellent thermal stability, high charge circulation. On account of the outstanding characteristic behavior of ILs, researchers have been inspired to use ILs for GO functionalization, by anchoring IL on the graphene surface functional groups [26–28]. Additionally, they took advantage of the positive effect of the imidazolium-based ILs by stabilizing Cr complexes. As a result, in this research, an imidazolium-based IL linker has been used to covalently attach Cr complex on the graphene sheet. Fortunately, the imidazolium-based IL, with its amino groups, basic and anionic nature appeared to be a good candidate for Cr(CO) complex formation.

1-Butyl-3-methylimidazolium chloride [BMIM]Cl has been used as an IL.

Other studies such as those conducted by D. Chen et al. [29] reported the use of reduced graphene oxide decorated  $\text{TiO}_2$  nanoparticles for hydrogen evolution by 3.45 times more than pure  $\text{TiO}_2$ . Thus, graphene materials as composite help  $\text{TiO}_2$  nanoparticles light absorption. This is due to its large surface area [30]. P. Wang et al. [31] demonstrated that the addition of RGO in the  $\text{TiO}_2$  improves the performance of  $\text{TiO}_2$  photocatalyst. In a study, the importance of graphene presence of semiconductor–carbon photocatalysts has been emphasized because of its unique role for selective oxidation [32]. However, the achievements on the application of  $\text{TiO}_2$ /GO or  $\text{TiO}_2$ /RGO for air purification have not been impressive, yet [33].

Herein, for the first time, the stabilization of Cr on  $\text{TiO}_2$ /IL-RGO to achieve an efficient photocatalyst for CO degradation has been reported. This method gives good results, as well as the reaction between Cr and carbonyl precursors in air.

## 2. Experimental

### 2.1. Reagents

Graphite (powder,  $<45\text{ }\mu\text{m}$ ,  $\geq 99.99\%$ , Sigma-Aldrich), potassium permanganate ( $\text{KMnO}_4$ , 158.03 g/mol, extra pure; Merck), sulfuric acid ( $\text{H}_2\text{SO}_4$  95%, extra pure, Merck), hydrogen peroxide ( $\text{H}_2\text{O}_2$  30%, Merck), sodium nitrate ( $\text{NaNO}_3$  84.99 g/mol,  $\geq 99.0\%$ , Merck), titanium isopropoxide  $\text{Ti}\{\text{OCH}(\text{CH}_3)_2\}_4$  (M.W. 284.22 g/mol<sup>-1</sup>) and 1-butyl-3-methylimidazolium chloride [BMIM]Cl ( $\geq 98.0\%$ ) were purchased from Sigma-Aldrich. Chromium(III) chloride anhydrous ( $\text{CrCl}_3$ , 158.35 g/mol, Merck), Benzyl chloride ( $\text{C}_7\text{H}_7\text{Cl}$  126.58 g/mol  $\geq 99.0\%$ , Merck), methanol ( $\text{CH}_3\text{O}$  32.04 g/mol, Merck) THF ( $\text{C}_4\text{H}_8\text{O}$  72.11 g/mol, Merck), and dilute hydrochloric acid (HCl 37% Merck diluted in  $\text{H}_2\text{O}$ ) were used in this research work.

### 2.2. Synthesis

#### 2.2.1. Preparation of the $\text{TiO}_2$ thin film

In this paper,  $\text{TiO}_2$  thin film was prepared using plasma enhanced CVD technique (PECVD) on quartz substrate. The pure titanium (IV) isopropoxide  $\text{Ti}\{\text{OCH}(\text{CH}_3)_2\}_4$  (TTIP) was used as Ti precursor and pure  $\text{O}_2$  (99.995%) was the working gas. RF generator operated at the frequency of 13.56 MHz and 300 W. The pressure in the main reactor was kept at high vacuum ( $10^{-6}$  Pa) before the deposition, utilizing turbo pump. Afterwards, the precursor was evaporated in an evaporator, at temperature 150 °C. The flow rates of TTIP vapor and oxygen were 0.24 sccm and 15 sccm, respectively. Last but not least important, mixed gases of Ar and  $\text{O}_2$  were purged to the vacuum chamber with a pressure ratio of 9:1 while the total pressure was 1.1 Pa. Quartz plates were rinsed in acetone and deionized water and then dried at 400 °C. The  $\text{TiO}_2$  film was deposited with the thicknesses of 100 nm during 20 min. Finally, these deposited films were annealed at 550 °C for 1 h in air.

#### 2.2.2. Preparation of GO

Graphene oxide (GO) was obtained from oxidation of graphite powder by Hummers method [34]. Typically, 2.00 g of graphite, 1 g of  $\text{NaNO}_3$  and 50 mL  $\text{H}_2\text{SO}_4$  were added into a 500 mL flask in an ice bath. Then the mixture was stirred for 15 min, after that, 6 g  $\text{KMnO}_4$  was added to the mixture during 1 h, followed by a stirring for an extra 2 h. 350 mL of deionized water was added into the mixture and stirred. The obtained mixture was left for 2 days at room temperature. Moreover, 20 mL of  $\text{H}_2\text{O}_2$  (30%) was added into the mixture, and finally cooled down to room temperature. For this test, the resulting precipitate was washed with dilute HCl (10%) several times before being dried under vacuum.

#### 2.2.3. Preparations of IL functionalized GO

In a typical reaction, 0.2 g GO mixed with 20 mL of 50 wt.% [BMIM]Cl in water, followed by sonication for 30 min and stirring at 100 °C for 2 h. The color of samples changed from dark brown to black, probably due to GO reduction. The functionalized GO was isolated by filtration and washed repeatedly several times with methylene chloride ( $4 \times 20$  mL) to remove the excess [BMIM]Cl and dried under vacuum.

#### 2.2.4. Stabilization of Cr complex on RGO/IL

The in-situ reduced and functionalized RGO with Cr, was obtained from the reaction of RGO/IL (0.2 g) with Benzyl chloride ( $\text{C}_7\text{H}_7\text{Cl}$ ) (0.1 mmol, 12.66 mg) and anhydrous  $\text{CrCl}_3$  (0.1 mmol, 15.83 mg) in methanol (50 mL). Subsequently, the mixture was refluxed for 1 h and then reserved for a few days at atmospheric temperature; green chrome-complex crystals of IL-Cr( $\eta^6\text{-C}_6\text{H}_5$ ) complex on RGO have emerged.

### 2.2.5. Deposition of functionalized GO on $TiO_2$

To obtain appropriate RGO/IL-Cr film, prepared RGO/IL-Cr was suspended in ethylene glycol (1 mg/mL). Then, the solution was sonicated with a probe-type sonicator for 15 min in order to obtain a uniform aqueous solution. The RGO/IL-Cr suspension was spin-coated at 1000 rpm for 2 min using a HOLMARC Spin coater-model: HO-TH-05 on PECVD deposited- $TiO_2$  surface. The resulting RGO/IL-Cr film thickness was  $50 \pm 2$  nm.

### 2.3. Instrumentation

UV-vis absorbance spectra and diffuse reflection spectroscopy (DRS) were recorded on an Avantes Avaspec-2048-TEC spectrometer in the wavelength range of 200–900 nm. The optical band gap,  $E_g$ , was obtained using the Tauc expression, by extrapolating the linear portion of  $(\alpha h\nu)^2$  as a function of the photon energy ( $h\nu$ ) [35]. Powder X-ray diffraction patterns were documented at 298 K on a PANalytical (X'Pert Pro MPD) system, using Cu anode, in the range of  $2\theta = 20\text{--}80^\circ$ . Accelerating voltage and applied current were running at 40 kV and 40 mA, respectively [36].

Fourier transform infrared (FT-IR) spectra were performed by Bruker tensor 27 using KBr pellets. It has been decided to script Raman spectroscopy measurements, using Horiba Jobin Yvon at  $\lambda = 532$  nm and employing laser power of 1.7 mW. Field-emission scanning electron microscopy (FESEM) (Tescan Mira2) was applied to gain data morphology of the samples. In addition to the above performance and before dealing with FESEM measurements, the sample surface was covered with a thin gold film to prevent charge build up. Transmission electron microscope (TEM) images of samples were recorded with Philips EM 208 microscope at 100 kV. X-ray photoelectron spectroscopy (XPS) was done on an X-ray photoelectron spectrometer (ESCALAB 250; VG Scientifics) under an Al  $K\alpha$  irradiation source (1486.7 eV) at 15 kV and 10 mA. A hemispherical energy analyzer (Specs EA 10 Plus, performing at  $10^{-7}$  Pa), was used to determine the core-level binding energies of photoelectrons emitted from the surface. Using the SDP software program (version 4.1) with 80% Gaussian–20% Lorentzian peak fitting, the peaks were shown totally deconvoluted. Furthermore, all binding energy (BE) values were calibrated by fixing the C (1s) core level with a BE of 285.0 eV. Brunauer–Emmett–Teller (BET) specific surface area test was performed using BEL Belsorp-Mini II 47, according to Adsorption–desorption isotherms of  $N_2$  at 77 K and relative pressure range of  $P/P_0 = 0.05\text{--}0.2$  [37].

Samples were degassed for 12 h at  $110^\circ\text{C}$  and  $10^{-6}$  Torr. Pore size dimensions were calculated using the Barrett–Joyner–Halenda (BJH) model according to the desorption branch of isotherm [38].

The thermal decomposition behavior was examined, using a Thermal Analysis (TA) TGA Q50, under a  $N_2$  purge from room temperature to  $800^\circ\text{C}$ , at a controlled heating rate of  $10^\circ\text{C min}^{-1}$ .

Ultimately, photocurrent properties were measured via an electrochemical analyzer (CHI 660D), in a three-electrode cell method. Pt wire acted as counter electrode. Ag/AgCl (in saturated KCl) was used as the reference electrode, and the prepared sample, coated on FTO conducting glass, performed as a working electrode, respectively. A 500W Xe arc lamp served as a light source.  $Na_2SO_4$  (0.5 mol L<sup>-1</sup>) aqueous solution was used as the electrolyte. Subsequently, working electrodes were prepared as follows: An FTO glass piece with a size of  $1.5 \times 9 \times 5$  cm was cleaned successively using acetone, boiled in  $NaOH$  (0.1 mol L<sup>-1</sup>), washed with deionized water and then dried in an air stream. The electrically conductive adhesive with a size of  $0.8 \times 9 \times 0.8$  cm was pressed on the bottom center of FTO glass. Finally, the sample powder was ground and closely compacted on the exposed electrically conductive adhesive. The light intensity was carefully fixed to  $100\text{ mW/cm}^2$  and the sample area exposed to light was  $0.5\text{ cm}^2$ .

### 2.4. Photocatalytic measurements

It is good to precise that the Photocatalytic reactor engaged for the research work was a batch reactor at room temperature. The prepared thin film photocatalyst plates were placed in the air-tight quartz photoreactor in front of constant UV lamp with an intensity of  $3.0\text{ mW/cm}^2$ . In fact, the thin-film photocatalysts contribute to the apparent surface area of  $50\text{ cm}^2$ . As the matter of fact, the vessel was placed under a UV lamp (8 W, OSRAM, Italy), to avoid temperature changing, one small ventilator was installed near the lamp. The assembled system was regularly checked for leaks, by applying a leak-test solution at every connection. Meticulously, Photocatalytic activity data was collected according to the degradation of carbon monoxide (CO), at ppm level. Analytical-grade CO was supplied from a compressed-gas stainless-steel cylinder of 50 ppmv ( $N_2$  balance, STG gas) with Messer gas regulator. The relative humidity of the flow was measured and controlled at 40%, using a water-filled Drechsel bottle. For a better precision, the flow rate was fixed at  $200\text{ mL/min}$  by a mass-flow controller. After fulfilling the adsorption–desorption equilibrium, the lamp was turned on. Finally, CO concentration was measured by a Modular gas analyzer (GMS800 gas analyzer, SICK), which monitors CO with a sampling rate of  $0.7\text{ L/min}$  (Fig. 1) [39,40].

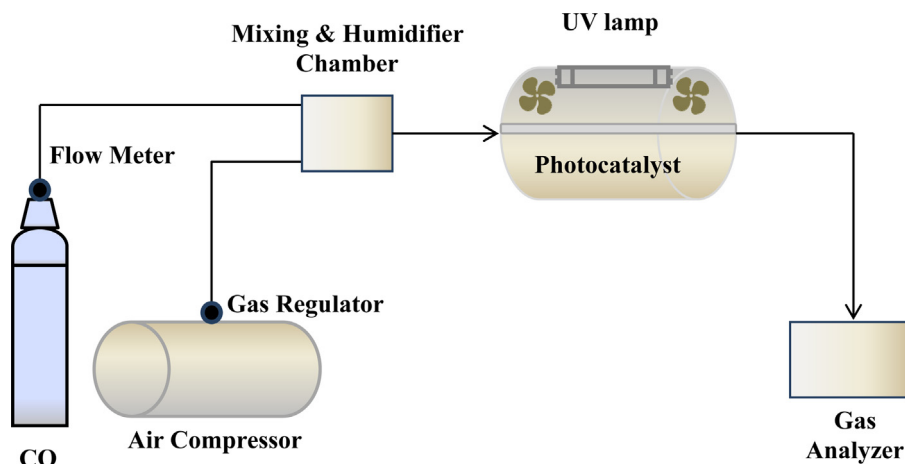
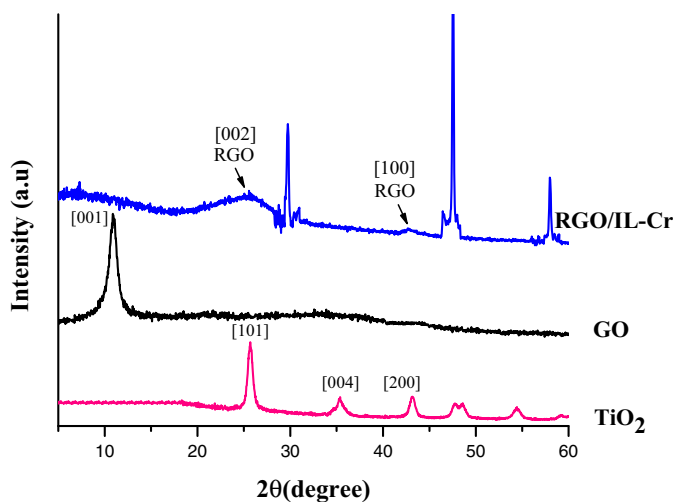


Fig. 1. Schematic laboratory setup for photocatalytic test measurements.



**Fig. 2.** XRD pattern of  $\text{TiO}_2$  thin film prepared by a PECVD technique, GO and RGO/IL-Cr nanocomposite.

### 3. Result and discussion

#### 3.1. Characterization

##### 3.1.1. XRD measurements

The X-ray diffraction (XRD) results of  $\text{TiO}_2$ , GO and nanocomposite of RGO/IL-Cr are shown in **Fig. 2**. In the XRD pattern of the  $\text{TiO}_2$

film deposited on quartz; main peaks are illustrated at  $25.3^\circ$ ,  $37.8^\circ$ , and  $48.6^\circ$ , which confirms the anatase phase with lattice planes of (101), (004), and (200), respectively [41–44].

In GO spectra, the characteristic peak at  $10.6^\circ$  (a d-spacing of  $7.62 \text{ \AA}$ ) confirms the nanosheet structure of GO and this is due to the presence of oxygenated functional groups. In the XRD pattern of prepared RGO/IL-Cr which was in-situ reduced, the characteristic peak at  $10.6^\circ$  corresponding to GO has been collapsed and instead of that, the diffraction peaks of RGO attributed to (002) and (100) are detected at  $22.6^\circ$  and  $42.5^\circ$ . The broad peaks, shifted to a higher angle, affirm the removal of surface oxy-functional groups and the complete reduction of GO. As seen from the XRD patterns, the sharp and vigorous peaks at  $2\theta$  of  $29.6^\circ$  (110),  $36.1^\circ$  (111) and  $42.41^\circ$  (200), emphasize the formation of cubic crystal of IL-Cr complex [45,46].

#### 3.1.2. FESEM and TEM images

The FESEM image of the  $\text{TiO}_2$  thin film deposited via PECVD route is presented in **Fig. 3a**. The image indicates the crystalline nature of the layer. The morphology of the particles is dense, resulting in mechanical strength increase. Besides, the surface coating is uniform without cracks [47]. In the FESEM image of GO in **Fig. 3b**, layered structure can be observed, which consists of ultrathin and homogeneous graphene sheets. On the other side, corresponding films are gently folded with ordered accumulation [48].

The morphology of composite RGO/IL-Cr shows large layered sheets (**Fig. 3c**). It can be seen that the surface of composite is smooth, with a little improvement in the structure. This may due to

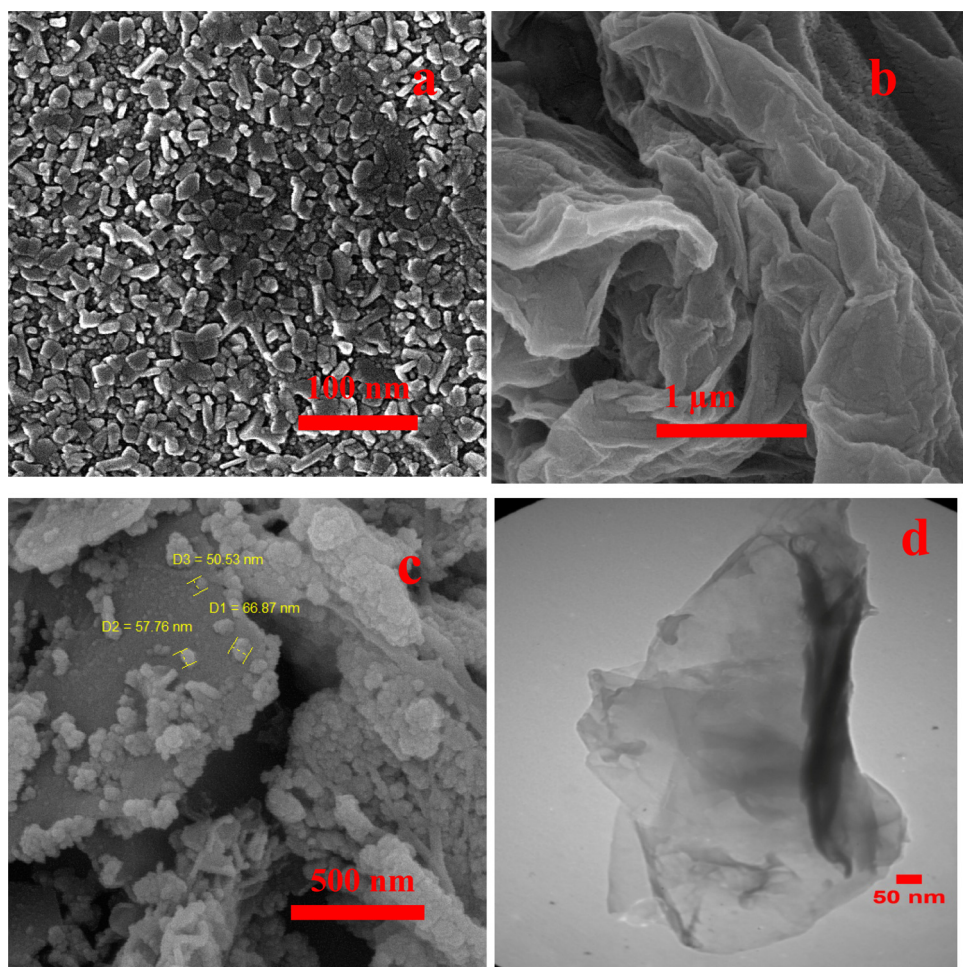


**Fig. 3.** (a) FESEM image of  $\text{TiO}_2$  thin layer deposited by PECVD technique, (b) FESEM image of GO, (c) RGO/IL-Cr and (d) TEM image of RGO/IL-Cr.

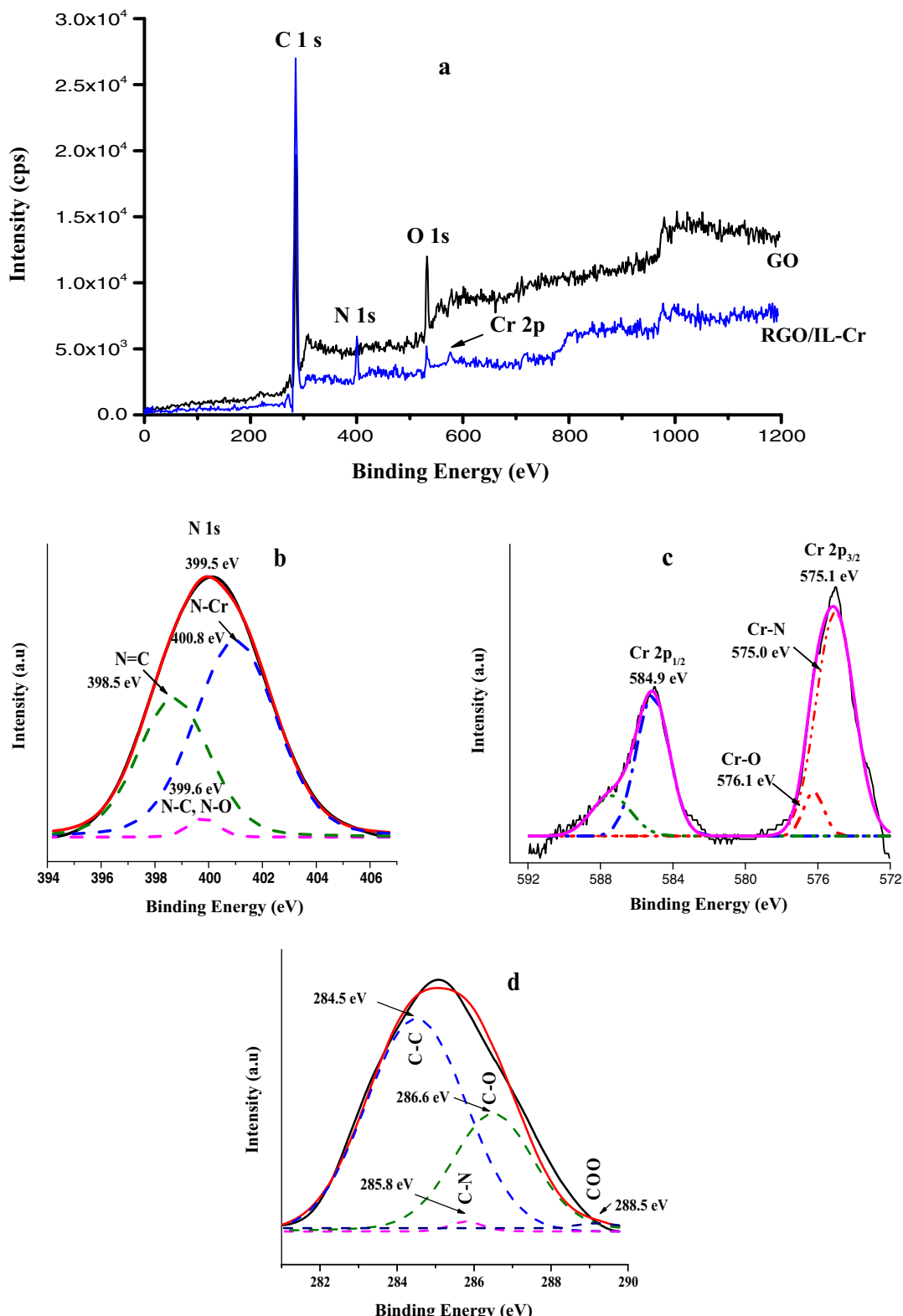


**Fig. 4.** (a) XPS full range spectra of GO and RGO-IL-Cr, (b) XPS high resolution spectra of N 1s with the curve-fitting results, (c) XPS high resolution region of Cr 3p with the results of curve-fitting and (d) C1s XPS high resolution spectrum with curve-fitting results.

the presence of IL between layers which avoids agglomeration. The small particles seen on graphene sheets are due to the attachment of IL-Cr functional groups on the surface of carbon grid.

Fig. 3d corresponds to TEM image of RGO/IL-Cr. As it is indicated in the image, the entire sheet is transparent and homogeneous [49].

### 3.1.3. Nitrogen adsorption–desorption isotherm

Fig. S1 (supporting information) illustrates the nitrogen adsorption–desorption isotherm of GO and RGO/IL-Cr at 77 K and at the saturated vapor pressure ( $P_0$ ) of 90.908 kPa.

According to the International Union of Pure and Applied Chemistry classification, the  $N_2$  adsorption-desorption isotherm of the two samples was type IV, with hysteresis loop type H3. A type IV adsorption-desorption isotherm indicates the presence of mesoporous, while a type H3 hysteresis loop, is in correlation with slit-shaped pores, possibly between parallel layers. The calculated BET Specific surface area ( $A_{BET}$ ) of GO is  $34.7 \text{ m}^2 \text{ g}^{-1}$ , with the average pore size of 6.0 nm. This is mainly due to the random stacking of GO sheets.

$A_{BET}$  for RGO/IL-Cr is  $312.2 \text{ m}^2 \text{ g}^{-1}$  which is about 10 times more than GO, due to the large number of oxygen removal during in-situ reduction, and replacement of small number of IL-Cr. The mean pore diameter of RGO/IL-Cr is 3.1 nm. The high  $A_{BET}$  has been exposed in more active sites and favored the mass transport of reactants and products [50,51].

### 3.1.4. TGA curves of GO and RGO/IL-Cr

The thermal properties of RGO/IL-Cr in comparison to GO are investigated by thermogravimetric analysis (TGA). The results are shown in Fig. S2 (supporting information). It can be seen that the thermal decomposition of RGO/IL-Cr is taken place below  $450^\circ\text{C}$ , as the main mass loss (ca. 60%) is derived from the decomposition of IL-Cr complex, from the RGO nanosheets. The TG analysis supported the successful modification of RGO with IL-Cr [52].

It is important to observe that pure GO is stable at lower temperature ( $<270^\circ\text{C}$ ). Only 10% of mass loss is obtained under  $100^\circ\text{C}$ , because of the evaporation of adsorbed water molecules. In consequence, the pyrolysis of GO is mainly occurred at around  $300^\circ\text{C}$  and finally mass loss of ca. 74% is achieved.

### 3.1.5. XPS analysis

Full range survey of X-ray photoelectron spectra (XPS) of GO and RGO/IL-Cr were carried out to ascertain the chemical composite of photocatalysts (Fig. 4a). The presence of main constituent elements Cr 2p (576.4 eV), N 1s (399.5 eV), C 1s (285.0 eV), O1s (532.2 eV) is on account of Cr and imidazolium IL in RGO/IL-Cr. In RGO/IL-Cr, the correlation of C to O peak area has relatively increased (6.1%), in comparison to 1.7% in GO, since oxygen functional groups have been decreased, after in-situ reduction.

A high-resolution N1s spectrum of RGO/IL-Cr is shown in Fig. 4b. The deconvoluted N1s spectrum assigns three different chemical states of N1s, according to literature. The main component in 400.8 eV corresponds to N–Cr. The peak contributed to N=C, is at 398.5 eV and the peak at 399.6 eV belongs to N–C.

High-resolution and deconvoluted peaks of Cr(III) (Cr 2p) in the RGO/IL-Cr catalysts are shown in Fig. 4c. The Cr 2p profile shows two main peaks at the position of 575.1 eV and 584.9 eV, assigned to Cr 2p<sub>3/2</sub> and Cr 2p<sub>1/2</sub>. It is noted that the Cr 2p<sub>3/2</sub> splits into two peaks of Cr–N (575.0 eV) and Cr–O (576.1 eV). Furthermore, the existence of Cr and IL may cause an improvement in catalytic activities [53–55].

High resolution XPS spectrum of C1s of RGO/IL-Cr is shown in Fig. 4d. In the spectrum, the noticeable, but little peak at around 288.5 eV is attributed to a small portion of remained carboxyl groups (0.9% of total C). This is due to the functionalization with the imidazolium IL in the composite. Furthermore, the appearance of a new peak at 285.8 eV (C–N) reveals the distinct chemical bonding of imidazolium N with graphene sheets [56].

### 3.1.6. Raman spectroscopy

Raman spectroscopy is a non-destructive and useful instrument to characterize graphene family materials, referring to their ordered carbon structure. In the GO spectrum shown in Fig. 5, two characteristic peaks at 1349 and 1597 cm<sup>-1</sup> are represented. These peaks are assigned to the D and G bands of the graphene, they are originated from the first-order scattering of the E2g phonon mode

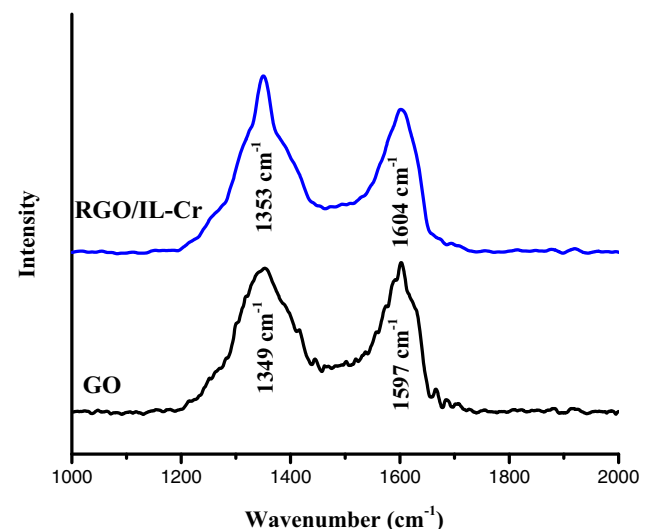


Fig. 5. Raman spectra of GO and RGO/IL-Cr.

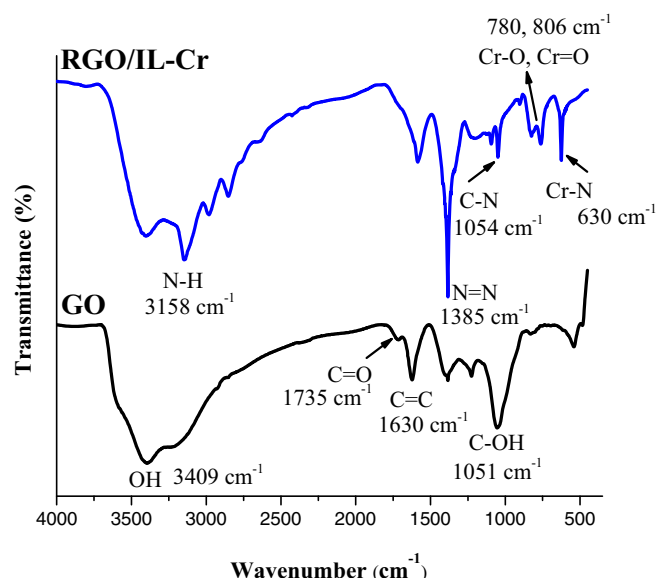


Fig. 6. FTIR spectra of GO and RGO/IL-Cr.

of sp<sup>2</sup>-hybridized C atoms and a symmetry A1g mode of k-point photons, appropriately. From the Raman spectra of RGO/IL-Cr, the presence of D or G bands indicates the ordered carbon framework remained after functionalization and reduction of GO. Furthermore, the G band of RGO/IL-Cr shifted from 1597 to 1604 cm<sup>-1</sup>, which further confirms that GO was successfully reduced. In RGO/IL-Cr, it is obvious that the D/G intensity ratio increased after reduction of GO, from 0.96 to 1.15. This higher value is due to the rise of defects in in-plane sp<sup>2</sup> size domains, in RGO [57].

### 3.1.7. FTIR spectroscopy

The in-situ reduction of GO for producing RGO/IL-Cr nanocomposite can be confirmed by the FT-IR. The FT-IR spectrum of GO, in Fig. 6, indicates a broad peak at 3409 cm<sup>-1</sup> together with a sharp peak at 1630 cm<sup>-1</sup>, corresponding to the stretching and bending vibration of water OH molecules, adsorbed on GO, respectively. The peak at 1735 cm<sup>-1</sup> which is assigned to C=O vibration in carboxylic acid and carbonyl groups on GO spectrum, disappears in the RGO/IL-Cr. Accordingly, C–OH bending at 1051 cm<sup>-1</sup> significantly

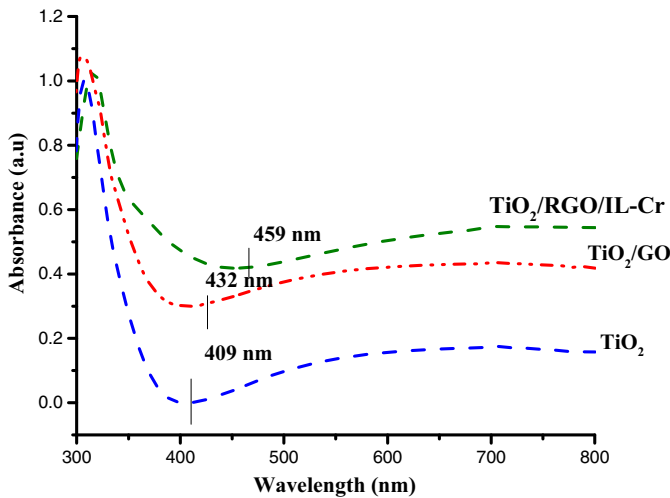


Fig. 7. UV-DRS spectra of  $\text{TiO}_2$ ,  $\text{TiO}_2/\text{GO}$ , and  $\text{TiO}_2/\text{RGO/IL-Cr}$  nanocomposite.

decreases, indicating that GO has been successfully reduced to RGO during the functionalization process [58–60].

In RGO/IL-Cr spectrum, the corresponding peaks of Imidazolium IL can be seen. The stretching vibration of the N–H group at  $3158\text{ cm}^{-1}$  is obvious and the peak at  $1385\text{ cm}^{-1}$  represents the stretching vibrations of N=N bond. The strong band at  $1054\text{ cm}^{-1}$  and medium band at  $1085\text{ cm}^{-1}$  are assigned to the C–N stretching vibrations. Furthermore, peaks at  $780$  and  $806\text{ cm}^{-1}$  correspond to the vibration of Cr–O and Cr=O. Similarly, the additional band in  $630\text{ cm}^{-1}$  is assigned to Cr–N, respectively, confirming the bonding of Cr with N and O in complex [61,62].

### 3.2. Optical properties

#### 3.2.1. UV-vis spectra and band-gap determination

UV-vis DRS spectra of  $\text{TiO}_2$ ,  $\text{TiO}_2/\text{GO}$ , and  $\text{TiO}_2/\text{RGO/IL-Cr}$  composites were recorded to study the optical absorption (Fig. 7). The synthesized  $\text{TiO}_2$  thin film spectrum edge has been located at around  $409\text{ nm}$  and corresponds to the charge transfer from the valence band of  $\text{O}^{2-}$  ions to the conduction band of  $\text{Ti}^{4+}$  ions. It has been noted that the calculated band gap for  $\text{TiO}_2$  is  $3.02\text{ eV}$ . Moreover,  $\text{TiO}_2/\text{GO}$  shows a redshift towards a higher wavelength ( $432\text{ nm}$ ). GO with oxygen functional groups, acts as a light absorbent, and the approximated band gap is  $2.77\text{ eV}$ . After addition of RGO/IL-Cr to  $\text{TiO}_2$ , the optical absorbance was shifted to a visible range ( $459\text{ nm}$ ) and the correlated band gap is  $2.64\text{ eV}$ . The redshift of optical absorbance can be explained as the result of band gap narrowness, with an addition of GO and RGO/IL-Cr. The high surface area of GO and RGO along with the presence of imidazolium and Cr in RGO/IL-Cr renders a strong light absorbance [63–66].

### 3.3. Photocatalytic activity towards removal of CO from air

#### 3.3.1. Photocatalyst pre-treatment

Before gas phase degradation reactions,  $\text{TiO}_2$ ,  $\text{TiO}_2/\text{GO}$  and  $\text{TiO}_2/\text{RGO/IL-Cr}$  film photocatalysts were pretreated with UV illumination. The irradiation occurred through purified air stream ( $5\text{ mL/min}$ ) in order to remove the adsorbed species such as water or surface impurities.

#### 3.3.2. Photocatalytic activity measurements

More tests were needed; a setup in batch-mode adsorption experiments was performed to check out the photocatalytic degradation of CO. To verify, the experiments were tested on five different

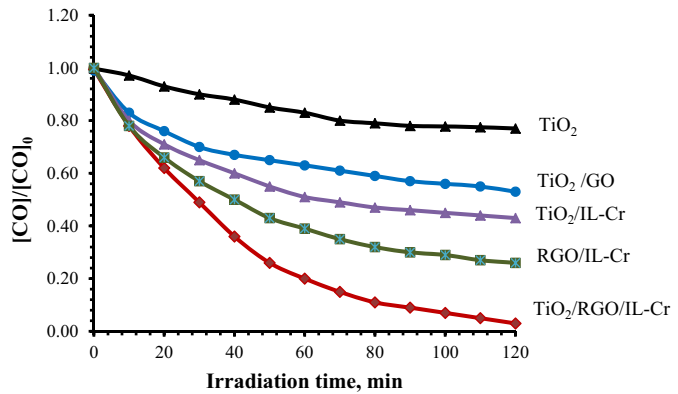


Fig. 8. Photodegradation of CO with irradiation time over five samples ( $\text{TiO}_2$ ,  $\text{TiO}_2/\text{GO}$ ,  $\text{TiO}_2/\text{IL-Cr}$ ,  $\text{RGO/IL-Cr}$  and  $\text{TiO}_2/\text{RGO/IL-Cr}$ ) under UV-light irradiation.

photocatalysts, such as pure  $\text{TiO}_2$  thin film,  $\text{TiO}_2/\text{GO}$ ,  $\text{TiO}_2/\text{IL-Cr}$ ,  $\text{RGO/IL-Cr}$  and  $\text{TiO}_2/\text{RGO/IL-Cr}$  nanocomposites.

Fig. 8 shows the photocatalysts performance for CO degradation ( $\text{C}/\text{C}_0$ ) under UV-light irradiation. In details, the initial concentration of CO, used in this study, was  $50\text{ ppmv}$ . It can be seen that only  $23\%$  degradation of CO was found, for a residence time of  $120\text{ min}$ , using the  $\text{TiO}_2$  thin-film photocatalyst. Regarding  $\text{TiO}_2/\text{GO}$  composite, the improved CO degradation of  $47\%$  was observed. As shown in Fig. 8, the conversion percentage of CO, using ternary composite of  $\text{TiO}_2/\text{IL-Cr}$ ,  $\text{RGO/IL-Cr}$  and  $\text{TiO}_2/\text{RGO/IL-Cr}$  photocatalysts, was calculated. Subsequently, after a residence time of  $120\text{ min}$ , using  $\text{TiO}_2/\text{IL-Cr}$  photocatalyst, near  $57\%$  oxidation of CO was obtained, comparing to  $72\%$  for  $\text{RGO/IL-Cr}$ , while the performance of  $\text{TiO}_2/\text{RGO/IL-Cr}$  for CO abatement was  $97\%$ . This reveals that the absorbed amount of gas on the  $\text{TiO}_2$  thin film, as starting material, is rather low. On contrary, it could be seen that the addition of GO and IL is effective, while the presence of RGO/IL-Cr increased the CO removal, definitely.

In the case of mixed gases, CO degradation on  $\text{TiO}_2$  thin film and  $\text{TiO}_2/\text{GO}$  has been reduced to  $5\%$ , whereas for  $\text{TiO}_2/\text{RGO/IL-Cr}$ , it was not changed, even in the same residence time. This is probably related to RGO/IL-Cr presence, which, on one hand increases CO adsorption and photodegradation, followed by an elevated production of hydroxyl radicals and in the other hand, IL-Cr complex can select CO for complex formation in mixed gases.

Influencing factors were investigated, in this purpose, narrow band gap of  $\text{TiO}_2/\text{GO}$  ( $2.77\text{ eV}$ ) and  $\text{TiO}_2/\text{RGO/IL-Cr}$  ( $2.64\text{ eV}$ ), were first considered to facilitate the photocatalytic reactions, in the composite.

Generally, GO and RGO have been synthesized by oxidation and reduction of graphite, this demonstrates the creation of valence band and conduction band, with the help of highest occupied molecular orbital (HOMO) and lowest unoccupied molecular orbital (LUMO). As a result, these materials have the potential to create sub-layer energy ( $\pi$  orbital) lower than the conduction band (d orbital) of  $\text{TiO}_2$ . This leads to the activation of the catalyst, under its original wavelength irradiation. In the present case the narrowing of the band gap can be the result of electronic transitions from intra-gap localized levels. These intra levels are located above the valence band up to the conduction band (Fig. 9) [67].

#### 3.3.3. Kinetic studies of CO photocatalytic degradation

In order to achieve the aspect for the scale up from the lab results, the photocatalytic activity for CO removal, is expressed in terms of kinetic studies. To develop the model, the reactor has been considered as a plug flow reactor (PFR) and the mass transport limitations from gas phase to solid phase, have been neglected. Regarding the first order reaction, the rate coefficient ( $r_A$ ) is inde-

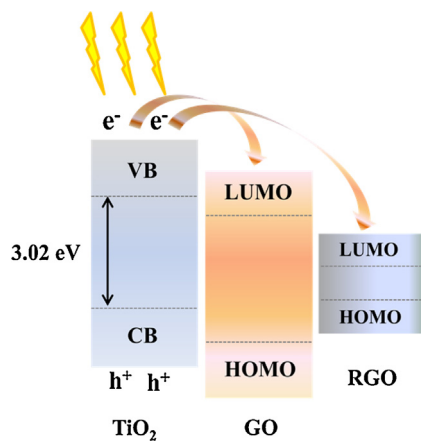


**Fig. 9.** Schematic diagram of gap reduction of  $\text{TiO}_2$  by photogenerated electron transferring to GO and RGO.

**Table 1**

First-order and second-order data calculated rate constants and  $R^2$  for photodegradation of CO.

Photocatalyst	CO Degradation Kinetic Data			
	First-order data		Second-order data	
	$K'$ ( $\text{min}^{-1}$ )	$R^2$	$K''$ [ $(\text{ppmv})^{-1} \cdot \text{min}^{-1}$ ]	$R^2$
$\text{TiO}_2$	0.0023	0.9977	$0.50 \times 10^{-4}$	0.9452
$\text{TiO}_2/\text{GO}$	0.0036	0.9993	$0.20 \times 10^{-3}$	0.9325
$\text{TiO}_2/\text{IL-Cr}$	0.0097	0.9981	$0.40 \times 10^{-3}$	0.8544
$\text{RGO}/\text{IL-Cr}$	0.0205	0.9990	$0.90 \times 10^{-3}$	0.9467
$\text{TiO}_2/\text{RGO}/\text{IL-Cr}$	0.0271	0.9993	$0.24 \times 10^{-2}$	0.9559

pendent from the flow rate  $Q$ . After determining concentration intergradations and volume limits, the first order model equation can be reached (Eqs. (1)–(3)) as follows:

$$QC_A dt = Q(C_A + dC_A) dt + (r_A) dVdt \quad (1)$$

$$r_A = -\frac{dC_A}{dt} = K'C_A \quad (2)$$

$$\ln\left(\frac{C_{A0}}{C_A}\right) = K'\tau \quad (3)$$

Where  $K'$  is the first-order reaction rate constant,  $(\tau)$  is residence time;  $C_{A0}$  and  $C_A$  are initial and ultimate CO concentrations at the photoreactor, respectively. The  $K'$  values have been reached by plotting  $\ln(C_{A0}/C_A)$  values versus  $\tau$  for the photodegradation of CO (Fig. 10a). The kinetic parameters of  $K'$  and  $R^2$  were obtained from the angular coefficient and linear adjustment of the line, respectively.

se procedure has been repeated for the second-order kinetic model theory, and  $K''$  (second-order constant) can be calculated from the linear slope of  $(1/C_A - 1/C_{A0})$  versus  $\tau$ . (Eqs. (4),(5)) (Fig. 10b) using the following equation:

$$r_A = -\frac{dC_A}{dt} = K''C_A^2 \quad (4)$$

$$\left(\frac{1}{C_A} - \frac{1}{C_{A0}}\right) = K''\tau \quad (5)$$

The corresponding experimental results for CO degradation are more adjusted to the pseudo-first order kinetic model. This is due to the fact that the values of  $R^2$ , obtained by the first-order kinetic model, are higher (0.9977–0.9993) than the second-order kinetic model (0.9325–0.9559) (Table 1). Hence, for implementing the rate constant for CO degradation, the first-order reaction plot is valid.

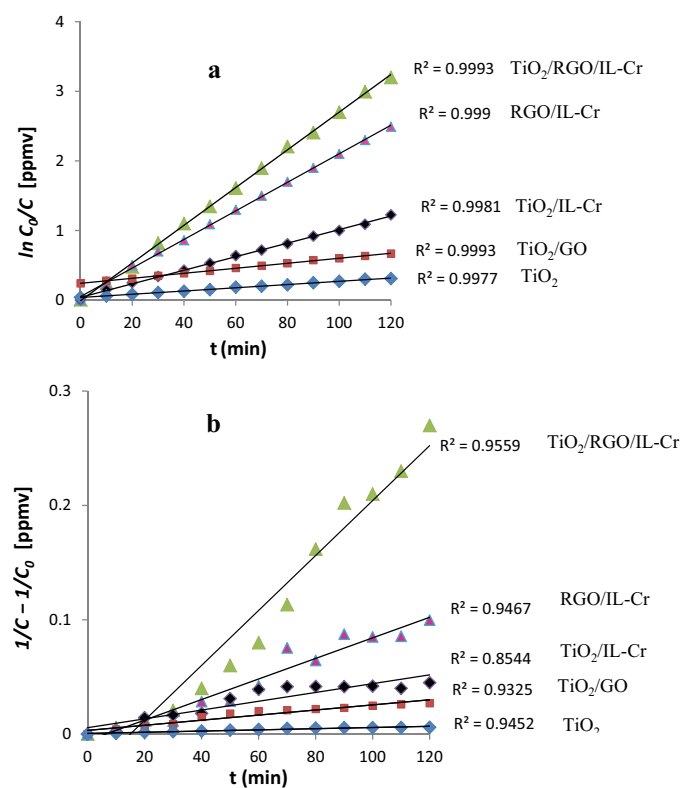


**Fig. 10.** (a) First-order kinetic model adjustment  $[\ln(C_0/C)]$  vs. illumination time (min) for CO degradation and (b) Second-order kinetic model adjustment  $[(1/C - 1/C_0)]$  vs. illumination time (min) for CO with different photocatalysts.

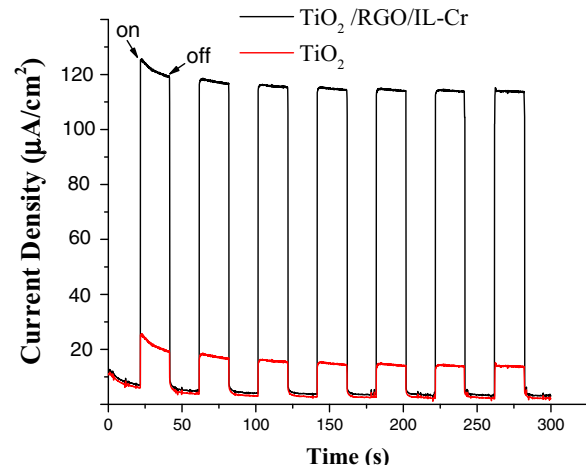


**Fig. 11.** Photocurrent transient responses of pure  $\text{TiO}_2$  and  $\text{TiO}_2/\text{RGO}/\text{IL-Cr}$  ternary composite.

### 3.3.4. Photocurrent studies

To better understand the origin of the superior photocatalytic performance of the  $\text{TiO}_2/\text{RGO}/\text{IL-Cr}$  ternary composite, the photocurrent time (PT) measurement was carried out. This method has been performed for suggesting a new photocatalytic mechanism and illustrating the synergistic effect between nanoparticles and graphene sheets. This demonstrates the interfacial charge separation for pure  $\text{TiO}_2$  and  $\text{TiO}_2/\text{RGO}/\text{IL-Cr}$  composite. As a consequence, the higher the photocurrent is, the higher the electron-hole ( $e^{-}_{cb} h^{+}_{vb}$ ) separation efficiency is, and thus the higher the photocatalytic activity is [68,69].

**Table 2**Photocatalytic reactions scheme for  $\text{TiO}_2/\text{RGO}/\text{IL-Cr}$ .

Excitation	$\text{TiO}_2 + h\nu \rightarrow \text{TiO}_2 (\text{e}^{-\text{cb}} + \text{h}^{+\text{vb}})$	(6)
Adsorption	$\text{GO}/\text{TiO}_2 + h\nu \rightarrow \text{GO} (\text{e}^{-\text{cb}})/\text{TiO}_2 (\text{h}^{+\text{vb}})$ $\text{RGO}/\text{TiO}_2 + h\nu \rightarrow \text{RGO} (\text{e}^{-\text{cb}})/\text{TiO}_2 (\text{h}^{+\text{vb}})$	(7) (8)
Recombination.	$\text{e}^{-\text{cb}} + \text{h}^{+\text{vb}} \rightarrow \text{Energy}$	(9)
Trapping	$\text{O}_{2\text{ads}} + \text{e}^{-\text{cb}} \rightarrow \bullet\text{O}^{-\text{2ads}}$ $\text{TiO}_2 (\text{h}^{+\text{vb}}) + \text{OH}_{\text{ads}}^- \rightarrow \text{OH}^\bullet$	(10) (11)
Reaction of other radicals	$\text{Cr}^{3+} + \text{e}^{-\text{cb}} \rightarrow \text{Cr}^{2+}$	(12)
CO oxidation	$\text{TiO}_2 + [\text{BMIM}]^+ + h\nu \rightarrow \text{TiO}_2 (\text{h}^{+\text{vb}}) + [\text{BMIM}]^+(\text{e}^{-\text{cb}})$ $\text{O}_2^\bullet + \text{e}^{-\text{cb}} + 2\text{H}^+ \rightarrow \text{H}_2\text{O}_2$ $\text{OH}^\bullet + \text{H}_2\text{O}_2 \rightarrow \text{HO}_2^\bullet + \text{H}_2\text{O}$ $2\text{OH}^\bullet + 2\text{CO} + 1/2\text{O}_2 \rightarrow 2\text{CO}_2 + \text{H}_2\text{O}$ $2\text{CO} + 2\text{HO}_2^\bullet \rightarrow 2\text{CO}_2 + \text{H}_2\text{O}$	(13) (14) (15) (16) (17)

**Fig. 11** shows the photocurrent-time testing curves of  $\text{TiO}_2$  and  $\text{TiO}_2/\text{RGO}/\text{IL-Cr}$  composite. It is obvious that  $\text{TiO}_2/\text{RGO}/\text{IL-Cr}$  sample is about 6 times higher photocurrent ( $120 \mu\text{A}/\text{cm}^2$ ) than pure  $\text{TiO}_2$  ( $20 \mu\text{A}/\text{cm}^2$ ), indicating that the composite holds stronger ability in separating photoinduced  $\text{e}^{-\text{cb}} \text{h}^{+\text{vb}}$  pairs. Higher generation of photocurrent from the excitation of electron–hole pairs, on the  $\text{TiO}_2/\text{RGO}/\text{IL-Cr}$  surface by light, can be explained by the following proposed mechanism; under light irradiation,  $\text{TiO}_2/\text{RGO}/\text{IL-Cr}$  nanoparticles undergo charge separation to yield electrons and holes. Because graphene sheets are known as good electron acceptors, while the holes are scavenged by the adsorbed water to form hydroxyl radicals, the electrons are quickly transferred to the graphene sheets and collected by the FTO electrode to generate photocurrent [70].

### 3.3.5. Photocatalytic CO degradation mechanism

In order to elucidate the catalytic reaction process, the corresponding mechanism is proposed for the photocatalytic reactions (Table 2). After appropriate light irradiation on  $\text{TiO}_2$ , the  $\text{e}^{-\text{cb}}$  and  $\text{h}^{+\text{vb}}$  pair is formed (Eq. (6)). The  $\text{e}^{-\text{cb}}$  and  $\text{h}^{+\text{vb}}$  pair can recombine quickly or may be adsorbed at the surface (Eqs. (7)–(10)). Since the  $\text{OH}_{\text{ads}}^-$  is likely available,  $\text{h}^{+\text{vb}}$  on the  $\text{TiO}_2$  surface, will react with  $\text{OH}_{\text{ads}}^-$  and generate  $\text{OH}^\bullet$  radicals (Eq. (11)). The super active  $\text{H}_2\text{O}_2$  and  $\text{HO}_2^\bullet$  radicals can be produced from  $\text{OH}^\bullet$  or  $\text{O}_2^\bullet$  radicals. (Eqs. (14), (15)).

By using surface adsorbents or charge trappers, the mobile species are separated and subsequently recombination may be avoided. Subsequently, GO and  $\text{RGO}/\text{IL-Cr}$  with high surface area ( $34.7, 312.2 \text{ m}^2 \text{ g}^{-1}$ ), are full of active sites for charge storage and can adsorb  $\text{e}^{-\text{cb}}$  (Eqs. (7), (8)) [71–73]. The  $\text{e}^{-\text{cb}}$  on the GO surface,

is captured by  $\text{O}_{2\text{ads}}$  to produce active  $\bullet\text{O}^{-\text{2ads}}$  and  $\text{H}_2\text{O}_2$  radicals (Eqs. (10), (14)). These photoactive radicals are responsible for the degradation of CO into less harmful  $\text{CO}_2$  (Eqs. (16), (17)) [74].

It can be seen that the high photocatalytic activity of the  $\text{TiO}_2/\text{RGO}/\text{IL-Cr}$  hybrid is also related to the functional groups (IL-Cr) on RGO surface. Obviously, XPS analysis of  $\text{RGO}/\text{IL-Cr}$ , confirmed the presence of imidazolium N atoms, which corresponds well to the previous proposed schemes for amine functionalized RGO as an  $\text{e}^{-\text{cb}}$  adsorbent [75].

Moreover, IL on the  $\text{TiO}_2/\text{RGO}/\text{IL-Cr}$  composite can absorb electrons ( $\text{e}^{-\text{cb}}$ ) by the cation head  $[\text{BMIM}]^+$ , according to electrostatic interactions [76]. Therefore, separation of photogenerated electrons and holes occurs on the surface of  $\text{TiO}_2$  (Eq. (13)). Based on this proposed mechanism,  $\text{Cr}^{3+}$  ions with high charge density can react with the  $\text{e}^{-\text{cb}}$  species as an electron scavenger, suppressing the electron/hole recombination (Eq. (12)) [77].

It is relevant to mention that the significant performance of  $\text{TiO}_2/\text{RGO}/\text{IL-Cr}$  nanocomposite relates to its  $\text{Cr}^{3+}$  ions.  $\text{Cr}^{3+}$  is a central atom in  $\text{IL-Cr}(\eta^6\text{-C}_6\text{H}_5)$ , which makes complexes with CO (coordinating agent) and produces  $[\text{Cr}(\text{CO})_3(\eta^6\text{-C}_6\text{H}_5)]$  (Eq. (18)).



**Fig. 12** represents the scheme of  $[\text{Cr}(\text{CO})_3(\eta^6\text{-C}_6\text{H}_5)]$  complex formation at the surface of RGO. This Cr(III) tricarbonyl arene complexes are stable according to the strong IL linker on RGO surface.

### 4. Conclusion

In summary, in this paper the hybrid photocatalyst was designed and created by anchoring Cr in the  $\text{TiO}_2$ /graphene oxide (GO)

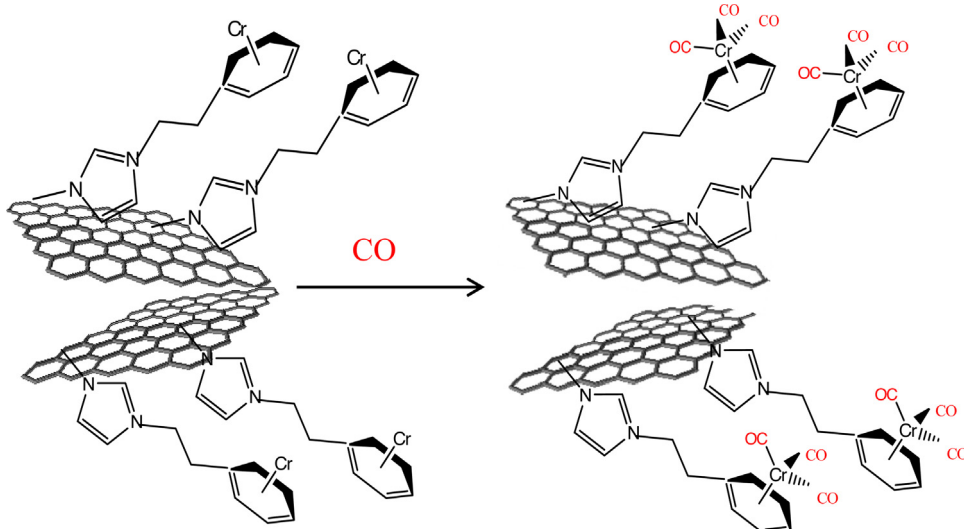


**Fig. 12.** Schematic diagram of  $\text{IL-Cr}(\eta^6\text{-C}_6\text{H}_5)$  and CO reaction to form  $[\text{Cr}(\text{CO})_3(\eta^6\text{-C}_6\text{H}_5)]$  complex on the surface of RGO.

composite. The reaction of 3-methylimidazolium (MIM) as an N-terminated ionic liquid (amine) with GO and afterwards, with benzyl chloride leads to produce an arene containing IL. Furthermore, direct reaction between chromium (Cr) and the IL resulted to the desired products. Besides, the X-ray photoelectron spectroscopy measurements along with other characterization methods, revealed the hybrid structure of Cr on RGO surface, with an imidazolium IL linker. The hybrid  $\text{TiO}_2/\text{RGO}/\text{IL-Cr}$  photocatalyst showed sustainable improved photocatalytic activity with 97% CO degradation, in 120 min residence time. The resultant Cr-arene material is appropriate for CO coordination  $[\text{Cr}(\text{CO})_3(\eta^6-\text{C}_6\text{H}_5)]$ .  $\text{TiO}_2/\text{RGO}/\text{IL-Cr}$  presented an enhanced photocatalytic activity and stability which was attributed to its high surface area of  $312.2 \text{ m}^2 \text{ g}^{-1}$  and its effective photogenerated charge carriers such as  $[\text{BMIM}]^+$  and  $\text{Cr}^{3+}$ , due to a delayed charge recombination. The advantage of coupling  $\text{TiO}_2$  with RGO-IL and Cr, allows the photocatalytic application for air purification.

## Appendix A. Supplementary data

Supplementary data associated with this article can be found, in the online version, at <http://dx.doi.org/10.1016/j.apcatb.2017.01.024>.

## References

- [1] H. Kobayashi, S. Higashimoto, *Appl. Catal. B: Environ.* 170 (2015) 135–143.
- [2] S. Dominguez, P. Ribao, M.J. Rivero, I. Ortiz, *Appl. Catal. B: Environ.* 178 (2015) 165–169.
- [3] S. Le, T. Jiang, Y. Li, Q. Zhao, Y. Li, W. Fang, M. Gong, *Appl. Catal. B: Environ.* 200 (2017) 601–610.
- [4] J.J. Murcia, E.G. Ávila-Martínez, H. Rojas, J.A. Navío, M.C. Hidalgo, *Appl. Catal. B: Environ.* 200 (2017) 469–476.
- [5] S. Ouyang, J. Ye, *J. Am. Chem. Soc.* 133 (2011) 7757–7763.
- [6] Y. Li, S. Ouyang, H. Xu, X. Wang, Y. Bi, Y. Zhang, J. Ye, *J. Am. Chem. Soc.* 138 (2016) 13289–13297.
- [7] H.U. Lee, S.C. Lee, S.H. Choi, B. Son, S.J. Lee, H.J. Kim, J. Lee, *Appl. Catal. B: Environ.* 129 (2013) 106–113.
- [8] A.A. Ismail, R.A. Geiushy, H. Bouzid, S.A. Al-Sayari, A. Al-Hajry, D.W. Bahnemann, *Appl. Catal. B: Environ.* 129 (2013) 62–70.
- [9] Y. Zhou, Y. Liu, P. Liu, W. Zhang, M. Xing, J. Zhang, *Appl. Catal. B: Environ.* 170 (2015) 66–73.
- [10] G. Xiao, X. Zhang, W. Zhang, S. Zhang, H. Su, T. Tan, *Appl. Catal. B: Environ.* 170 (2015) 255–262.
- [11] C. Dette, M.A. Pérez-Osorio, C.S. Kley, P. Punke, C.E. Patrick, P. Jacobson, F. Giustino, S.J. Jung, K. Kern, *Nano Lett.* 14 (2014) 6533–6538.
- [12] S.S.R. Putluru, L. Schill, A.D. Jensen, B. Siret, F. Tabaries, R. Fehrmann, *Appl. Catal. B: Environ.* 165 (2015) 628–635.
- [13] S. Karapati, T. Giannakopoulou, N. Todorova, N. Boukos, D. Dimotikali, C. Trapalis, *Appl. Catal. B: Environ.* 176 (2015) 578–585.
- [14] Z. Wei, F. Liang, Y. Liu, W. Luo, J. Wang, W. Yao, Y. Zhu, *Appl. Catal. B: Environ.* 201 (2017) 600–606.
- [15] M. Pelaez, N.T. Nolan, S.C. Pillai, M.K. Seery, P. Falaras, A.G. Kontos, P.S.M. Dunlop, J.W.J. Hamilton, J.A. Byrne, K. O'Shea, M.H. Entezari, D.D. Dionysiou, *Appl. Catal. B: Environ.* 125 (2012) 331–349.
- [16] US. EPA. Quantitative Risk and Exposure Assessment for Carbon Monoxide –Amended. U.S. Environmental Protection Agency, Research Triangle Park, North Carolina, EPA –452/R-10-009 (2010).
- [17] X. Yu, F. Zhang, W. Chu, *RSC Adv.* 6 (2016) 70537–70546.
- [18] N. Seifvand, E. Kowsari, *RSC Adv.* 5 (2015) 93706–93716.
- [19] M. Rosillo, G. Domínguez, J. Pérez-Castells, *Chem. Soc. Rev.* 36 (2007) 1589–1604.
- [20] R. Saada, S. Kellici, T. Heil, D. Morgan, B. Saha, *Appl. Catal. B: Environ.* 168 (2015) 353–362.
- [21] W. Liu, J. Cai, Z. Ding, Z. Li, *Appl. Catal. B: Environ.* 174 (2015) 421–426.
- [22] Y. Zhang, C. Zhong, Q. Zhang, B. Chen, M. He, B. Hu, *RSC Adv.* 5 (2015) 5996–6005.
- [23] Y. Cen, Y. Yao, Q. Xu, Z. Xia, R.D. Sisson, J. Liang, *RSC Adv.* 6 (2016) 66971–66977.
- [24] S. Zhu, Y. Dong, X. Xia, X. Liu, H. Li, *RSC Adv.* 6 (2016) 23809–23815.
- [25] M. Roso, A. Lorenzetti, C. Boaretti, D. Hrelja, M. Modesti, *Appl. Catal. B: Environ.* 176 (2015) 225–232.
- [26] Y. Huang, Y. Wang, Y. Wang, Q. Pan, X. Ding, K. Xu, N. Lia, Q. Wen, *RSC Adv.* 6 (2016) 5718–5728.
- [27] E. Aliyari, M. Alvand, F. Shemirani, *RSC Adv.* 6 (2016) 64193–64202.
- [28] B. Lin, T. Feng, F. Chu, S. Zhang, N. Yuan, G. Qiao, J. Ding, *RSC Adv.* 5 (2015) 57216–57222.
- [29] D. Chen, L. Zou, S. Li, F. Zheng, *Sci. Rep.* 6 (20335) (2016), <http://dx.doi.org/10.1038/srep20335>.
- [30] W. Wang, J. Yu, Q. Xiang, B. Cheng, *Appl. Catal. B: Environ.* 119 (2012) 109–116.
- [31] P. Wang, J. Wang, X. Wang, H. Yu, J. Yu, M. Lei, Y. Wang, *Appl. Catal. B: Environ.* 132 (2013) 452–459.
- [32] M. Yang, N. Zhang, Y.J. Xu, *ACS Appl. Mater. Interfaces* 5 (2013) 1156–1164.
- [33] Y. Zhang, Z.-R. Tang, X. Fu, Y.-J. Xu, *ACS Nano* 4 (2010) 7303–7314.
- [34] W.S. Hummers, R.E. Offeman, *J. Am. Chem. Soc.* 80 (1958), 1339–1339.
- [35] J. Tauc, *Optical Properties of Solids*, North-Holland, Amsterdam (1972).
- [36] C. Suryanarayana, M. Grant Norton, *X-Ray Diffraction: A Practical Approach*, Plenum Press, New York, 1998.
- [37] K.S.W. Sing, D.H. Everett, R.A.W. Haul, L. Moscou, R.A. Pierotti, J. Rouquerol, T. Siemieniewska, *Pure Appl. Chem.* 57 (1985) 603–619.
- [38] F. Rouquerol, J. Rouquerol, K. Sing, *Adsorption by Powders & Porous Solids*, Academic Press, London, 1999.
- [39] C.H. Huang, I.K. Wang, Y.M. Lin, Y.H. Tseng, C.M. Lu, *J. Mol. Catal. A: Chem.* 316 (2010) 163–170.
- [40] ISO 10677: 2011, *Fine Ceramics, Advanced Technical Ceramics –Ultraviolet Light Source for Testing Semiconducting Photocatalytic Materials*, ISO, Geneva, 2011.
- [41] C. Liu, T. Sun, L. Wu, J. Liang, Q. Huang, J. Chen, W. Hou, *Appl. Catal. B: Environ.* 170 (2015) 17–24.
- [42] Y. Liu, W. Yao, X. Cao, X. Weng, Y. Wang, H. Wang, Z. Wu, *Appl. Catal. B: Environ.* 160 (2014) 684–691.
- [43] P. Apopei, C. Catrinescu, C. Teodosiu, S. Royer, *Appl. Catal. B: Environ.* 160 (2014) 374–382.
- [44] F. Dufour, S. Pigeot-Remy, O. Durupthy, S. Cassaignon, V. Ruaux, S. Torelli, L. Mariéy, F. Maugeé, C. Chanéac, *Appl. Catal. B: Environ.* 174 (2015) 350–360.
- [45] J. Wang, Y. Lv, Z. Zhang, Y. Deng, L. Zhang, B. Liu, R. Xu, X. Zhang, *J. Hazard. Mater.* 170 (2009) 398–404.
- [46] S. Sarkar, S. Niyogi, E. Bekyarova, R.C. Haddon, *Chem. Sci.* 2 (2011) 1326–1333.
- [47] P. Hájková, J. Matoušek, P. Antoš, *Appl. Catal. B: Environ.* 160 (2014) 51–56.
- [48] W. Li, J. Liu, C. Yan, *Carbon* 55 (2013) 313–320.
- [49] H. Lv, Y. Liu, J. Hu, Z. Li, Y. Lu, *RSC Adv.* 4 (2014) 63238–63245.
- [50] T. Li, N. Li, J. Liu, K. Cai, M.F. Foda, X. Lei, H. Han, *Nanoscale* 7 (2015) 659–669.
- [51] A. Trapalis, N. Todorova, T. Giannakopoulou, N. Boukos, T. Speliotis, D. Dimotikali, *Jiaguo Yu, Appl. Catal. B: Environ.* 180 (2016) 637–647.
- [52] H.-H. Chun, W.-K. Jo, *Appl. Catal. B: Environ.* 180 (2016) 740–750.
- [53] Y.-S. Wang, J.-H. Shena, J.-J. Horng, J. Haz. Mat. 274 (2014) 420–427.
- [54] M.C. Biesinger, B.P. Payne, A.P. Grosvenor, L.W.M. Lau, A.R. Gerson, R.St.C. Smart, *Appl. Surf. Sci.* 257 (2011) 2717–2730.
- [55] O.C. Compton, B. Jain, D.A. Dikin, A. Abouimrane, K. Amine, S.T. Nguyen, *ACS Nano* 5 (2011) 4380–4391.
- [56] C. Botas, P. Álvarez, C. Blanco, R. Santamaría, M. Granda, P. Ares, F. Rodríguez-Reinoso, R. Menéndez, *Carbon* 50 (2012) 275–282.
- [57] X. Zeng, Z. Wang, N. Meng, D.T. McCarthy, A. Deletic, J. Pan, X. Zhang, *Appl. Catal. B: Environ.* 202 (2017) 33–41.
- [58] W. Ye, X. Shi, J. Su, Y. Chen, J. Fu, X. Zhao, F. Zhou, C. Wang, D. Xue, *Appl. Catal. B: Environ.* 160 (2014) 400–407.
- [59] L. Ye, Z. Li, *Appl. Catal. B: Environ.* 160 (2014) 552–557.
- [60] E.M. Rodríguez, G. Márquez, M. Tena, P.M. Álvarez, F.J. Beltrán, *Appl. Catal. B: Environ.* 178 (2015) 44–53.
- [61] A.S.K. Kumar, T. Gupta, S.S. Kakani, S. Kalidhasan, V. Manasi, N. Rajesh, J. Hazard. Mater. 239 (2012) 213–224.
- [62] A.S.K. Kumar, N. Rajesh, *RSC Adv.* 3 (2013) 2697–2709.
- [63] H. Li, Z. Xia, J. Chen, L. Lei, J. Xing, *Appl. Catal. B: Environ.* 168 (2015) 105–113.
- [64] T.K. Le, D. Flahaut, H. Martinez, H.K.H. Nguyen, T.K.X. Huynh, *Appl. Catal. B: Environ.* 165 (2015) 260–268.
- [65] S.-S. Chen, H.-C. His, S.-H. Nian, C.-H. Chiu, *Appl. Catal. B: Environ.* 160 (2014) 558–565.
- [66] L.-L. Tan, W.-J. Ong, S.-P. Chai, B.T. Goh, A.R. Mohamed, *Appl. Catal. B: Environ.* 179 (2015) 160–170.
- [67] D. Zhao, G. Sheng, C. Chen, X. Wang, *Appl. Catal. B: Environ.* 111 (2012) 303–308.
- [68] W.-K. Jo, S. Kumar, M.A. Isaacs, Adam F. Lee, S. Karthikeyan, *Appl. Catal. B: Environ.* 201 (2017) 159–168.
- [69] W. Fan, X. Yu, H.-C. Lu, H. Bai, C. Zhang, W. Shi, *Appl. Catal. B: Environ.* 181 (2016) 7–15.
- [70] X. Men, H. Chen, K. Chang, X. Fang, C. Wu, W. Qin, S. Yin, *Appl. Catal. B: Environ.* 187 (2016) 367–374.
- [71] V. Trevisan, A. Olivo, F. Pinna, M. Signoretto, F. Vindigni, G. Cerrato, C.L. Bianchi, *Appl. Catal. B: Environ.* 160 (2014) 152–160.
- [72] S. Chowdhury, R. Balasubramanian, *Appl. Catal. B: Environ.* 160 (2014) 307–324.
- [73] C.C. Pei, W.W.-F. Leung, *Appl. Catal. B: Environ.* 175 (2015) 515–525.
- [74] H. Wang, T. Yu, X. Tan, H. Zhang, P. Li, H. Liu, L. Shi, X. Li, J. Ye, *Ind. Eng. Chem. Res.* 55 (2016) 8096–8103.
- [75] Y. Nie, W.-N. Wang, Y. Jiang, J. Fortner, P. Biswas, *Catal. Sci. Technol.* 6 (2016) 6187–6196.
- [76] N. Seifvand, E. Kowsari, *Ind. Eng. Chem. Res.* 55 (2016) 10533–10543.
- [77] A. Meng, J. Xing, Z. Li, Q. Li, *ACS Appl. Mater. Interfaces* 7 (2015) 27449–27457.